strike-slip Sierran frontal fault system (*29*).

In the model, we also implicitly assume that the thermal structure of the crustal section is homogeneous. Heterogeneities in the thermal structure will be produced by continued extension of the upper crust, such that the geothermal gradient will eventually be higher immediately below the rift basin. For this reason, flank volcanism appears to be related most clearly to the early phases of extension, and later volcanism erupts through the axial zones of rifts (*4–6*).

Despite the foregoing qualifications, flank volcanism has been noted by field geologists in many environments and has seemed to defy simple explanation. The explanation we offer is simple and consistent with a model that explains other mechanical features of normal faulting (*1*). We assume that melt with some mantle affinities exists in parts of the lower crust. Such a hypothesis is consistent with recent observations that minor hot spots resulting from mantle processes are much more numerous on the Pacific floor than previously believed (*30*). Similar processes occurring beneath continents would provide the magma sources we hypothesize.

REFERENCES AND NOTES

1. G. King and M. Ellis, *Nature* **348**, 689 (1990).
2. I. A. Nairn and S. Beanland, *N. Z. J. Geol. Geophys.* **32**, 1 (1988).
3. C. J. N. Wilson and G. P. L. Walker, *Philos. Trans. R. Soc. London Ser. A* **314**, 199 (1985).
4. C. J. Ebinger, A. L. Deino, R. E. Drake, A. L. Tesha, *J. Geophys. Res.* **94**, 15785 (1989).
5. B. C. King, in *East African Magmatism*, I. Gass, Ed. (Oliver and Boyd, Edinburgh, 1970), pp. 263–282.
6. P. Mohr, *Tectonophysics* **143**, 169 (1987), and references therein; W. H. Morton, D. C. Rex, J. G. Mitchell, P. Mohr, *Nature* **280**, 284 (1979).
7. S. Horton and D. dePolo, personal communication.
8. D. P. Hill *et al.*, *Bull. Seismol. Soc. Am.* **80**, 325 (1990).
9. R. A. Bailey, *U.S. Geol. Surv. Open-File Rep. 77-468* (1977). Geothermal studies (including analysis of gravity and drill hole data) suggest that the original frontal fault system was farther to the east, placing Mammoth Mountain and associated volcanic centers unequivocally in the footwall [G. A. Suemnicht and R. J. Varga, *J. Geophys. Res.* **93**, 13191 (1988)].
10. B. R. Julian, *Nature* **303**, 323 (1983).
11. ———, *J. Geophys. Res.* **90**, 11155 (1985).
12. J. O. Langbein, D. P. Hill, T. N. Parker, S. K. Wilkinson, A. M. Pitt, *Eos* **43**, 1466 (1990).
13. W. Hildreth and G. A. Mahood, *Geol. Soc. Am. Bull.* **97**, 396 (1986).
14. P. W. Lipman, *Trans. R. Soc. Edinburgh Earth Sci.* **79**, 265 (1988), and references therein.
15. A. I. Kiselev, *Tectonophysics* **143**, 235 (1987) ———, H. A. Golovko, M. E. Medvedev, *ibid.* **45**, 49 (1978).
16. R. G. Bohannon, C. W. Naeser, D. L. Schmidt, R. A. Zimmerman, *J. Geophys. Res.* **94**, 1683 (1989).
17. R. E. Anderson, *Geol. Soc. Am. Abstr. Program* **20**, A115 (1988).
18. C. B. Hunt and D. R. Mabey, *U.S. Geol. Surv. Prof. Pap. 494-A* (1966).
19. G. W. Grindley, *Philos. Trans. R. Soc. London Ser. A* **274**, 165 (1973).
20. Carte Geologique de la France et de la Marge Continentale, Bureau de Recherche Geologique et Minière BP 6009, 45066, Orléans, Cedex.
21. The upper crust was modeled as an elastic plate with a density of 2700 kg m^{-3}, a thickness of 12 km, a crustal Young's modulus of 40 GPa, and an effective elastic thickness of ~3 km. The lower crust was assumed inviscid, with a density of 2900 kg m^{-3}. We further assumed 80% erosion and sedimentation at the earth's surface and an initial fault dip of 60°.
22. G. C. P. King, R. Stein, J. Rundle, *J. Geophys. Res.* **93**, 13307 (1988); R. Stein, G. C. P. King, J. Rundle, *ibid.*, p. 13319; R. G. Bilham and G. C. P. King, *ibid.* **94**, 10204 (1989).
23. D. A. Spence and D. L. Turcotte, *ibid.* **90**, 575 (1985); J. R. Lister and R. C. Kerr, *ibid.* **96**, 10049 (1991); A. M. Rubin and D. D. Pollard, *U.S. Geol. Surv. Prof. Pap. 1350* (1987), p. 1449.
24. J. M. Bartley, J. M. Fletcher, A. F. Glazner, *Tectonics* **9**, 521 (1990).
25. L. A. Wright *et al.*, *Geological Society of America Field Trip Guidebook* (Geological Society of America, Boulder, CO, in press).
26. W. Bosworth, *Geology* **15**, 397 (1987).
27. N. White, *ibid.* **17**, 111 (1989). White [*ibid.* **18**, 327 (1990)] also shows that simple-shear models of lithospheric extension make it extremely difficult to generate melt from the asthenosphere. W. R. Buck, F. Martinez, M. S. Steckler, S. R. Cochran, *Tectonics* **7**, 213 (1988); T. H. Dixon, E. R. Ivins, B. J. Franklin, *ibid.* **8**, 1193 (1989). In general, the simple-shear model advocated originally by B. Wernicke [*Can. J. Earth Sci.* **22**, 108 (1985)] has been superseded by models that involve more distributed shear within the lower crust [for example, G. S. Lister and G. A. Davis, *J. Struct. Geol.* **11**, 65 (1989)], to the extent that the Moho remains flat while the middle or lower crust is fluid [see (*1*) and B. Wernicke, in *Exposed Cross-Sections of the Continental Crust*, M. H. Salisbury and D. M. Fountain, Eds. (Kluwer Academic, Boston, 1990)].
28. C. J. Ebinger, T. D. Bechtel, D. W. Forsyth, C. O. Bowin, *J. Geophys. Res.* **94**, 2883 (1989). Estimates of effective elastic thickness determined from the geometry of footwall–hanging wall pairs along the western arm of the East African rift are of the order of 4 km [N. Kusznir and R. Westaway, *Eos* **71**, 1584 (1990)], which is close to that determined by King and Ellis (*1*) for the Basin and Range province, but in contrast to that of Ebinger's estimation.
29. M. Bursik and K. Sieh, *J. Geophys. Res.* **94**, 15587 (1989).
30. L. Fleitout and C. Moriceau, *Geophys. J. Int.*, in press.

31. This work was started while M. Ellis was at the Center for Neotectonic Studies, University of Nevada, Reno, and was supported then and while G. King was at the U.S. Geological Survey, Denver, CO, by the Nevada Nuclear Waste Projects Office. We are particularly grateful to R. E. Anderson, R. Thompson, R. Schweickert, B. Julian, R. Stein, and W. Mooney for insightful and constructive criticism and D. Matthews for editorial assistance.

3 June 1991; accepted 31 July 1991

Theoretical Fermi-Surface Properties and Superconducting Parameters for K_3C_{60}

STEVEN C. ERWIN AND WARREN E. PICKETT

Quantitative theories of superconductivity in alkali-doped C_{60} require an accurate and detailed description of the Fermi surface. First-principles calculations of Fermi-surface properties and electronic parameters for K_3C_{60}, the prototype fulleride-superconductor, are reported. The Fermi surface has two sheets; the first is free-electron-like, and the second is multiply-connected, forming two interlocked symmetry-equivalent pieces that never touch. The calculated (clean limit) London penetration depth is $\Lambda = 1600$ Å. Comparing the Fermi velocity with the experimental coherence length leads to a superconducting pairing strength $\lambda \sim 5$, indicating very strong coupling. Partial nesting in the second Fermi-surface sheet may favor coupling to short-wavelength $\langle q,0,0\rangle$ optic modes.

IT IS NOW WELL ESTABLISHED THAT alkali-doping of C_{60} fullerenes leads to a class of solids, M_xC_{60} (M = alkali), that exhibit at least four crystalline phases, corresponding to $x = 0,3,4,6$. Theory and experiment show that both undoped C_{60} and fully-doped M_6C_{60} are molecular insulators, with predicted band gaps of 1.5 eV (*1*) and 0.5 eV (*2*), respectively. In striking contrast, M_3C_{60} forms a metallic superconducting phase, with transition temperatures (T_c) ranging from 18 K (M = potassium) (*3*) to 28 K (M = rubidium) (*4*), and even higher for Cs-Rb alloys (*5*). Recent theoretical attention has focused on electron-phonon coupling as a possible mechanism for superconductivity (*6, 7*). It is well known that the coupling strength and critical temperature are strongly influenced by zone-averaged electronic properties, such as the Fermi-level density of states. However, the shape of the Fermi surface may also play a significant role, by giving rise to wavevector anisotropies in the quasiparticle-pairing strength, as for the La_2CuO_4-based superconductors (*8*). Here we report the results of our first-principles calculations of the Fermi surface and of electron dynamics in K_3C_{60}, and of the coupling strength λ implied by our results and experimental data.

Rietveld analysis of powder x-ray diffraction data for K_3C_{60} reveals a simple face-centered cubic (fcc) Bravais lattice, with K atoms located at the tetrahedral and octahedral interstitial sites (*9*). The best fit was achieved with C_{60} molecules placed randomly in two orientations, each populated

S. C. Erwin, Department of Physics, University of Pennsylvania, Philadelphia, PA 19104–6272.
W. E. Pickett, Complex Systems Theory Branch, Code 4692, Naval Research Laboratory, Washington, DC 20375–5000.

by 50%. Carbon atoms were determined to be within 0.02 Å of their ideal positions. The lattice constant is 14.24 Å, nearly identical to the lattice constant of the undoped phase, 14.11 Å.

The best-fit structure of Stephens *et al.* (*9*) is a disordered one that is beyond the current capabilities of first-principles electronic-structure methods; it may also not reflect all the details of the true structure. The two orientations of the C_{60} molecule leave the intermolecular nearest-neighbor C-C distances and bond angles nearly unchanged; thus the intermolecular hopping, which primarily determines the band structure, is unaltered. For this reason, we use an idealized structure in which only a single orientation of C_{60} molecules is allowed, resulting in a point-group symmetry of T_h within a fcc Bravais lattice.

Our calculations use the local-density approximation to density-functional theory. The all-electron charge density and potential are determined self-consistently and without shape approximation. The basis set consists of gaussian functions contracted into atomic orbitals, plus a number of additional single Gaussian functions; further details may be found in a recent study (*2*) of K_6C_{60}. The density-of-states (DOS) and Fermi surface are determined by diagonalizing the Hamiltonian at 61 k-points uniformly distributed throughout the irreducible 1/24 of the Brillouin zone, then Fourier-interpolating these energies to denser meshes.

The resulting electronic band structure and DOS for K_3C_{60} are shown in Fig. 1. The highest occupied set of three bands, with t_{1u} symmetry at Γ (p-like with respect to the center of the C_{60} cage), is half-filled by three electrons (one from each K atom). The band width W is 0.6 eV, and the total DOS for both spins, $N(E)$, shows two distinct peaks. The Fermi level, E_F, sits on the high-energy slope of the lower peak, with $N(E_F) = 13.2$ states/eV-cell. The calculated Fermi velocity, $v_F = 1.8 \times 10^7$ cm s^{-1}, leads to a Drude plasma energy $\hbar\Omega_p = 1.2$ eV and a London penetration depth (in the clean limit) $\Lambda = c/\Omega_p = 1600$ Å; the latter compares reasonably well with the initial reported value (*10*) of 2400 Å, and less well with the value of 4800 Å from muon-spin relaxation (*11*). For a dirty superconductor (that is, one in which the mean free path is shorter than the $T = 0$ coherence length), Λ is increased by a factor $(1 + \xi/l)^{1/2}$, where l is the mean free path. For the minimum possible value of $l \sim 10$ Å (the C_{60} separation) and the experimental coherence length (*10*), $\xi = 26$ Å, this factor is nearly 2, bringing the calculated value of Λ in the dirty limit into better agreement with experiment. Using our value for v_F, the experimental value $T_c = 19.3$ K (*10*), and the standard expression $\xi = \hbar v_F/\pi\Delta$ to calculate the superconducting gap parameter Δ, one finds the BCS ratio $2\Delta/k_BT_c = 17$. Using instead Allen's formula (*12*)

$$\xi = \sqrt{\frac{7}{4}\zeta(3)}\,\frac{\hbar v_F}{2\pi k_B T_c(1+\lambda)} \qquad (1)$$

one finds the pairing strength $\lambda = 5.3$. Although they seem unusually large, these values for λ and the Barden-Cooper-Schrieffer (BCS) ratio definitely imply strong coupling. If a phonon mechanism is responsible, then superconductivity results from very strong coupling to medium- or low-frequency modes, rather than from weak coupling to the very high frequency internal vibrations of the C_{60} molecule (which would require only modest values of λ and a normal BCS ratio of 3.52).

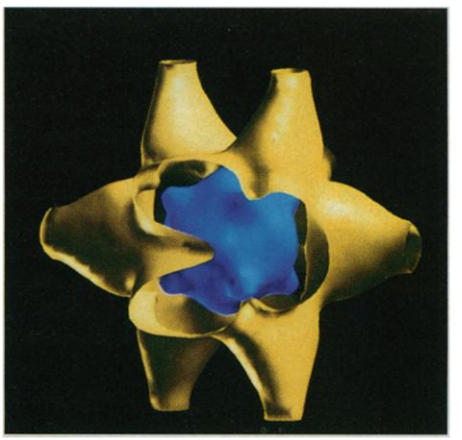

Fig. 2. First (blue) and second (yellow) sheets of the K_3C_{60} Fermi surface, each enclosing unoccupied states. Part of the second sheet is cut away to reveal the first sheet inside.

As we noted earlier, we assume a single orientation of C_{60} molecules, in contrast to the best-fit structure of Stephens *et al.* (*9*). The Drude plasma energy should be insensitive to such differences. $N(E_F)$ and v_F could be somewhat more sensitive; however, $N(E_F)$ is not far from the average value $\langle N(E)\rangle = 6$ electrons/$W = 10$ states/eV-cell, so these quantities should also be relatively insensitive to such details.

Two of the three t_{1u} bands cross the Fermi

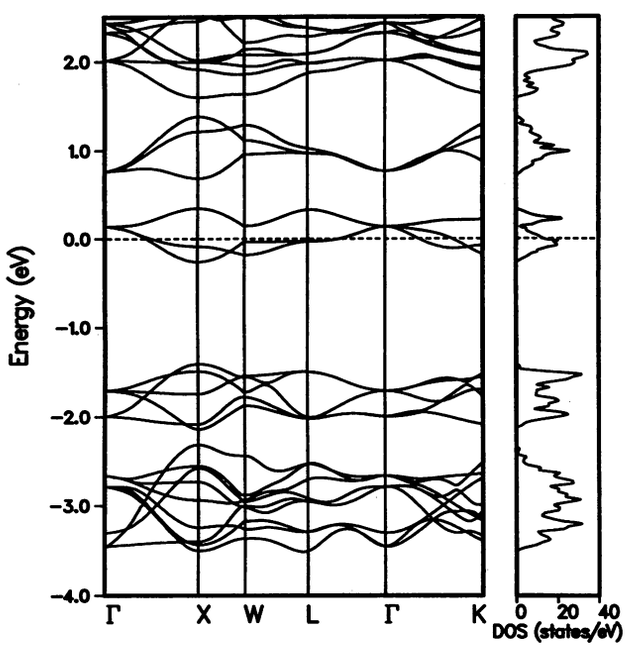

Fig. 1. Self-consistent electronic band structure of K_3C_{60}. The zero of energy is defined by the Fermi level. The density of states (DOS) is for both spins combined.

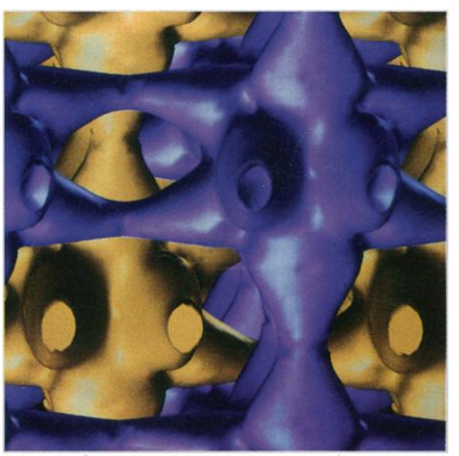

Fig. 3. Repeated-zone representation for the second sheet of the Fermi surface for K_3C_{60}, which holds the charge carriers that become superconducting. The two symmetry-equivalent pieces (shown in different colors) are multiply connected along Cartesian axes; although interpenetrating, they never touch.

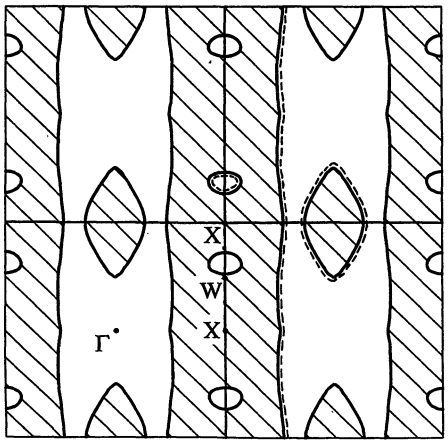

Fig. 4. Repeated-zone representation, in the k_z = 0 plane, of the second Fermi-surface sheet; occupied regions are cross-hatched. Several extremal electron and hole orbits are indicated by dotted curves.

Table 1. De Haas–van Alphen frequencies f and cyclotron effective masses m^*/m for the extremal orbits in K_3C_{60}. Orbits for ⟨100⟩ fields on the second Fermi-surface (FS) sheet are sketched in Fig. 4.

FS sheet	Orbit center	Particle	Field direction	f(MG)	m^*/m
1	Γ	Hole	⟨100⟩	64	2.2
1	Γ	Hole	⟨110⟩	70	3.1
2	~(W+X)12	Hole	⟨100⟩	6	0.6
2	X	Electron	⟨100⟩	46	1.9
2	Γ	Hole	⟨100⟩	178	8.4

level, hence the Fermi surface has two sheets (Fig. 2). The first sheet is a distorted sphere centered at Γ, enclosing hole states, with a mean radius of $0.4(2\pi/a)$. Small protrusions extend outward in the ⟨111⟩ directions, to make contact with the second sheet, which shows similar inward protrusions; these points of contact arise from the symmetry degeneracy of the two lower bands all along the ⟨111⟩ directions. The second sheet of the Fermi surface is open, and is considerably more complex (see Fig. 3). Also enclosing hole states, the second sheet is multiply-connected along Cartesian ⟨100⟩ directions. Since connections are made not to nearest-neighbor zones (which are in the ⟨111⟩ directions), but rather to next-nearest-neighbor zones, this has the unusual consequence of generating two identical multiply-connected Fermi surfaces; although interlinked, the two pieces are distinct. The connections themselves also show a novel structure, consisting of thick necks that split into thin double-tubes at a distance of $0.25(2\pi/a)$ from the ⟨100⟩ zone boundaries. It is noteworthy that this double-tube structure would not be possible under O_h symmetry, and thus is a striking consequence of the point-group symmetry of the crystal being lowered to T_h by the icosahedral symmetry of the C_{60} molecules.

The two Fermi-surface sheets give rise to a variety of possible orbits, some of which are sketched in Fig. 4: closed hole orbits (first and second sheets), closed electron orbits (second sheet), and open orbits (second sheet). For the extremal closed orbits, we have calculated (Table 1) the de Haas–van Alphen frequencies, $f = (\hbar c/e)A$, and cyclotron effective masses, $m^*/m = (\hbar^2/2\pi m)\partial A/\partial E$, where A is an extremal cross-sectional area. Note that although the frequencies are very small compared with those of simple metals (for example, 105 MG for the "neck" orbit, and 3100 MG for the "belly" orbit of Au), this is primarily a consequence of A^{-1} scaling with the square of the lattice constant; indeed, the ratios of largest to smallest frequencies are nearly identical.

The strength of pairing for two quasiparticles on the Fermi surface, mediated by a boson of wavevector $\mathbf{Q}$, is strongly affected by the phase space available for scattering $\mathbf{k} \rightarrow \mathbf{k} + \mathbf{Q}$, in which both $\mathbf{k}$ and $\mathbf{k} + \mathbf{Q}$ are required to lie on the Fermi surface:

$$\xi_{nm}(\mathbf{Q}) = N^{-1}\sum_{\mathbf{k}}\delta(E_{n,\mathbf{k}} - E_F)\delta(E_{m,\mathbf{k}+\mathbf{Q}} - E_F) \quad (2)$$

where n and m are band indices. If a squared electron-phonon matrix element is inserted into the sum, the result is the coupling strength of the phonon $\mathbf{Q}$ to quasiparticles on the Fermi surface. $\xi_{nm}(\mathbf{Q})$ has significant contributions only from intraband transitions on the second Fermi-surface sheet; Fig. 5 shows a contour plot of $\xi_{22}(\mathbf{Q})$, which reveals nesting features on this sheet that make transitions near $\mathbf{Q} = \langle w,0,0\rangle 2\pi/a$, for $0.5 < w \leq 1.0$, more important than for the average phonon. These peaks indicate that short-wavelength vibrations involving {100} planes of C_{60} molecules and cations moving against one another receive preferential phase space.

Our results provide fundamental information that will be important for a theory of superconductivity in fullerides. The bandwidth, W = 0.6 eV, is small; using the tight-binding expression $W = 2zt$ (z = coordination number) leads to a very small inter-cage hopping parameter, $t \sim 50$ meV. This value results from the very large inter-cage minimum C-C distance of 3.12 Å (more than twice the intra-cage C-C separation), and implies a relatively long residence time for a carrier on a C_{60} molecule. However, the large lattice constant results in values of ν_F and $N(E_F)$ that are not so different from conventional superconductors. Vibrational frequencies in fullerides range up

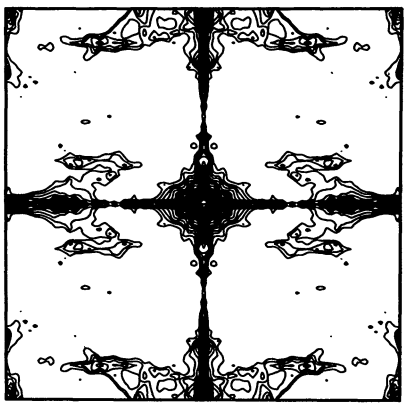

Fig. 5. Contour plot of $\xi_{22}(\mathbf{Q})$ in the Q_z = 0 plane of the first Brillouin zone. Substantial enhancements in the phase-space factor are evident in the narrow regions along Cartesian directions near the outer part of the zone. (The singularity at the zone center arises from the definition of $\xi_{nm}(\mathbf{Q})$, and has no physical significance.)

to ω_{max} = 1600 cm^{-1} (0.2 eV) for the intra-cage vibrations. Since $\hbar\omega_{max}$ is of the order of the occupied bandwidth, $W/2$ = 0.3 eV, one can anticipate the breakdown of the adiabatic approximation; the treatment of electron-phonon interactions then becomes no easier than for electron-electron interactions.

The question of which phonons might be most important is already a topic of discussion. Stollhoff (7) and Martins *et al.* (*13*) have argued that the high-energy internal bond-stretching modes should be most effective in coupling carriers. Zhang *et al.* (*14*) advocate the importance of the K^+-ion optic modes. The small value of t derived above suggests other modes will cause strong coupling. Since t is small, the overlap of C atomic orbitals from neighboring C_{60} molecules will be in the exponentially decreasing regime; thus, motions that modulate the inter-cage hopping should greatly affect the band structure, that is, show strong electron-phonon coupling, and would be reflected most strongly in transport behavior. Two such types of phonons are short-wavelength modes involving (i) vibrations of neighboring C_{60} molecules against one another, and (ii) rotational modes of C_{60} molecules. The large mass and moment of inertia of the C_{60} molecule will lead to relatively low energies and large displacements. We caution, however, that the long residence time and suspected large polarizability of the C_{60} molecule may result in unusual electron-electron interactions, and the current strong focus on electron-phonon coupling may therefore be premature.

REFERENCES AND NOTES

1. S. Saito and A. Oshiyama, *Phys. Rev. Lett.* **66**, 2637 (1991).

2. S. C. Erwin and M. R. Pederson, *ibid.* **67**, 1610 (1991).
3. A. F. Hebard *et al.*, *Nature* **350**, 600 (1991).
4. M. J. Rosseinsky *et al.*, *Phys. Rev. Lett.* **66**, 2830 (1991).
5. K. Tanigaki *et al.*, *Nature* **352**, 222 (1991); S. P. Kelty, C.-C. Chen, C. M. Lieber, *ibid.*, p. 223.
6. P. J. Benning, J. L. Martins, J. H. Weaver, L. P. F. Chibante, R. E. Smalley, *Science* **252**, 1417 (1991).
7. G. Stollhoff, in preparation.
8. W. E. Pickett, H. Krakauer, R. E. Cohen, *Physica B* **165 & 166**, 1055 (1990).
9. P. W. Stephens *et al.*, *Nature* **351**, 632 (1991).
10. K. Holczer *et al.*, *Phys. Rev. Lett.* **67**, 271 (1991).
11. Y. J. Uemura *et al.*, *Nature* **352**, 605 (1991).
12. P. B. Allen, in *Modern Trends in the Theory of Condensed Matter: Proc. XVI Karpacz Winter School of Theoretical Physics*, A. Pekalski and J. Przystawa, Eds. (Springer-Verlag, New York, 1980), pp. 388–413.
13. J. L. Martins, N. Troullier, M. Schabel, in preparation.
14. F. C. Zhang, M. Ogata, T. M. Rice, in preparation.
15. Partial support is acknowledged from the Office of Naval Research. Calculations were performed on the IBM 3090 at the Cornell National Supercomputing Facility.

9 September 1991; accepted 26 September 1991

Modulation of the Affinity of Integrin $\alpha_{IIb}\beta_3$ (GPIIb-IIIa) by the Cytoplasmic Domain of α_{IIb}

TIMOTHY E. O'TOOLE, DAVID MANDELMAN, JANE FORSYTH, SANFORD J. SHATTIL, EDWARD F. PLOW, MARK H. GINSBERG*

Intracellular signaling alters integrin adhesive functions in inflammation, immune responses, hemostasis, thrombosis, and retinal development. By truncating the cytoplasmic domain of α_{IIb}, the affinity of integrin $\alpha_{IIb}\beta_3$ for ligand was increased. Reconstitution with the cytoplasmic domain from integrin α_5 did not reverse the increased affinity. Thus, the cytoplasmic domain of the α subunit of GPIIb-IIIa controls ligand binding affinity, which suggests mechanisms for inside-out transmembrane signaling through integrins. These findings imply the existence of hitherto unappreciated hereditary and acquired thrombotic disorders in humans.

INTEGRIN-MEDIATED ADHESION participates in diverse biological processes such as development, inflammation, wound repair, and hemostasis (*1*). The cellular repertoire of integrins and the availability of adhesive ligands control these processes. In addition, integrin function is dynamically regulated by cells in response to developmental signals (*2*), cell-cell interactions (*3*), or soluble agonists (*4*). Integrin adhesive functions are controlled by their affinity for ligands. For example, $\alpha_{IIb}\beta_3$ (GPIIb-IIIa) (*4*) or $\alpha_M\beta_2$ (Mac-1) (*5*) bind soluble fibrinogen (Fg) only after cellular stimulation. In $\alpha_{IIb}\beta_3$, this affinity change is due to alterations in the conformation of the receptor (*6*).

Intracellular signal transduction that involves G proteins, calcium, phospholipid metabolism, and kinases (*7*) is implicated in affinity modulation of integrins, but the link between these pathways and changes in receptor conformation has remained elusive. The putative cytoplasmic domains of α and β subunits are topographically accessible to intracellular signals and may therefore mediate these affinity changes. To test this possibility, we have examined the effect of truncations of the cytoplasmic domains of $\alpha_{IIb}\beta_3$ on its affinity state. This integrin was chosen because dynamic changes in its affinity (*4*) and ligand binding specificity (*8*) are readily assayed by use of Fg or an activation-specific monoclonal antibody (MAb), PAC1 (*9*), which binds to an epitope that is only revealed after activation.

Truncated α_{IIb} and β_3 subunits were generated by in vitro mutagenesis (*10*); the truncated α_{IIb} ($\alpha_{IIb}\Delta991$) retained two residues of the putative cytoplasmic domain, whereas the truncated β_3 ($\beta_3\Delta728$) retained six residues (Fig. 1A). Chinese hamster ovary (CHO) cell lines that expressed these constructs were analyzed by immunoprecipitation of surface-labeled cells (Fig. 1B) with site-specific antisera to the extracellular domain of α_{IIb} (amino acids 859 to 871) (*11*) and the cytoplasmic domains of α_{IIb} (amino acids 989 to 1008) and β_3 (amino acids 742 to 762) (Fig. 1B). The wild-type $\alpha_{IIb}\beta_3$ was immunoprecipitated with all three antisera. In contrast, $\alpha_{IIb}\beta_3\Delta728$ was immunoprecipitated with anti-α_{IIb}(859–871) and anti-α_{IIb}(989–1008), but not with anti-β_3(742–762). Conversely, $\alpha_{IIb}\Delta991\beta_3$ was precipitated by anti-α_{IIb}(859–871) and anti-β_3(742–762), but not by anti-α_{IIb}(989–1008). A double truncation, $\alpha_{IIb}\Delta991$–$\beta_3\Delta728$, was immunoprecipitated with anti-α_{IIb}(859–871), but not with the cytoplasmic domain antibodies.

The affinity state of $\alpha_{IIb}\beta_3$ in these cell lines was initially characterized by the binding of the MAb PAC1 (Fig. 2). This anti-$\alpha_{IIb}\beta_3$ interacts selectively with the active, not the inactive, receptor and presumably binds at or near the ligand binding pocket, because its interaction competes with typical $\alpha_{IIb}\beta_3$ ligands (*12*). The $\alpha_{IIb}\beta_3$ and $\alpha_{IIb}\beta_3\Delta728$ transfected cells did not bind PAC1 specifically unless they were activated

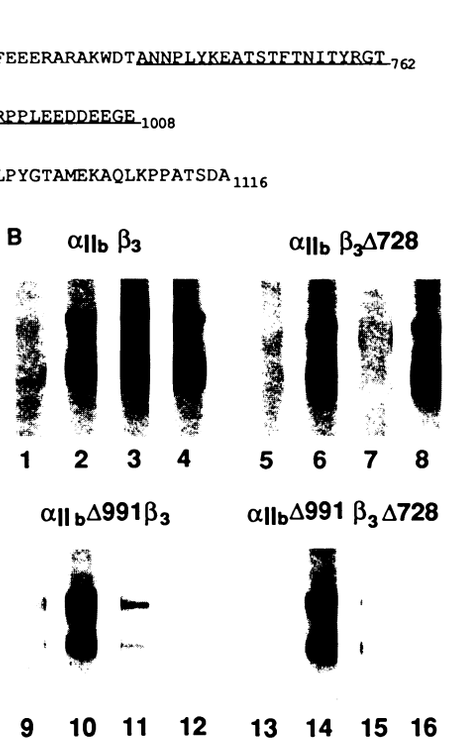

Fig. 1. $\alpha_{IIb}\beta_3$ truncation in CHO cells. (**A**) The partial transmembrane (bold) and complete cytoplasmic amino acid sequence for wild-type (WT) or variant α_{IIb} and β_3 constructs. The subscripts denote residue number, whereas the underlined sequences denote peptide immunogens for cytoplasmic domain–specific antisera. Single letter abbreviations for the amino acid residues: A, Ala; C, Cys; D, Asp; E, Glu; F, Phe; G, Gly; H, His; I, Ile; K, Lys; L, Leu; M, Met; N, Asn; P, Pro; Q, Gln; R, Arg; S, Ser; T, Thr; V, Val; W, Trp; and Y, Tyr. (**B**) Wild-type or truncated α_{IIb} and β_3 subunits were identified by immunoprecipitation from extracts of surface-labeled cells. Cells were labeled with ^{125}I and then lysed and immunoprecipitated as described (*6*) with polyclonal antisera to an extracellular portion of α_{IIb}(859–871) (*11*) and the cytoplasmic domains of α_{IIb}(989–1008) and β_3(742–762). Immunoprecipitates were resolved by SDS–6% polyacrylamide gels electrophoresis and analyzed by autoradiography. Lanes 1, 5, 9, and 13, preimmune serum; lanes 2, 6, 10, and 14, anti-α_{IIb}(859–871); lanes 3, 7, 11, and 15, anti-β_3(742–762); and lanes 4, 8, 12, and 16, anti-α_{IIb}(989–1008).

T. E. O'Toole, D. Mandelman, J. Forsyth, E. F. Plow, M. H. Ginsberg, Committee on Vascular Biology, The Scripps Research Institute, La Jolla, CA 92037.
S. J. Shattil, University of Pennsylvania Cancer Center, Philadelphia, PA 19104.

*To whom correspondence should be addressed.